材料の環境劣化の３次元的理解のための手法としての FIB シーケンシャルセクショニング法

FIB sequential sectioning as a tool to understand environmental materials degradation in 3D

S Lozano-Perez *1, N Ni *1, K Kruska *1, T Terachi *2 and T Yamada *2

要約 近年，自動化機構が改良されたデュアル・カラム FIB-SEM は，連続的に取得した画像を，３次元再構築することを可能にした．この技術の原子炉材料の環境劣化領域での適用は，相や欠陥に対して３次元的な特徴を nm の解像度で表現することが可能である．本報告では，表面酸化，き裂の発生，耐酸化性に及ぼす冷間加工の影響，溶接金属のき裂成長を含む，同手法の適用例を示す．

キーワード FIB-SEM，３次元キャラクタリゼーション，環境劣化，酸化，き裂成長

Abstract In the recent years, the arrival of dual column FIB-SEMs and their improved level of automation has enabled the sequential acquisition of images that can be used to reconstruct sample volumes in 3D. When applied to the area of environmental degradation of materials in nuclear reactors, it can become a very powerful technique, capable of represent in 3D features, phases and/or defects with nm resolution. Examples of application include the characterization of surface oxidation and crack initiation in austenitic alloys, effects of cold work in oxidation resistance and crack growth in welded 316L stainless steel.

Keywords FIB-SEM, 3D characterization, environmental degradation, oxidation, crack growth

1. Introduction

Most phenomena associated to environmental materials degradation occur in 3D although a complete 3D characterization is rarely possible. In the last decade, developments in several techniques have enabled the acquisition of better 3D data and a considerable narrowing of the quality and resolution gap that separates 2D from 3D. These techniques include X-ray tomography, where sub-micron resolution is nowadays easily achieved and can provide with chemical and microstructural information [(1)(2)]; XPS, AES and SIMS in the form of depth-profiling combined with mapping[(3)～(5)]; Scanning Transmission Electron Microscopy tomography [(6)] and Atom-probe tomography[(7)]. 3D focused ion beam (FIB) slicing or FIB sequential slicing has been recently used to characterize crack morphologies[(8)] but still has not exploited its full potential to characterize environmental degradation. In this work, through three examples of application, we will demonstrate that FIB sequential slicing is to become a key technique if 3D information is to be extracted with high spatial resolution and minimum sample preparation.

2. Materials and methods

2.1 Materials

Various alloys with important degradation issues have been selected to illustrate the power of FIB sequential sectioning. These include:

1. A commercial stress-relieved ZIRLO™ alloy (0.89% Sn, 0.09% Fe, 0.87% Nb, 0.01% Cr, bal.

＊1 Department of Materials, Oxford University, Parks Road, Oxford, OX1 3PH, UK.
＊2 Institute of Nuclear Safety System (INSS), 64 Sata, Mihama-cho, Mikata-gun, Fukui 919-1205, Japan

Zr), which was oxidized in simulated PWR primary water in an autoclave at 360℃ for 3360h. This alloy is used as a cladding material for the nuclear fuel in light water reactors.

2. A 304SS with prior 20% cold work (by cold rolling), which was oxidized in simulated PWR primary water in an autoclave at 340℃ for 1500h. This alloy can be found in the primary circuit of light water reactors.

3. A welded 316L with prior 20% cold work (by cold rolling), which was oxidized in simulated PWR primary water in an autoclave at 320℃ for 648h. This alloy can be found in the primary circuit of light water reactors.

2.2 Methods

FIB sectioning was carried out on a Zeiss NVision 50 dual beam FIB instrument (2-30kV Ga + incident beam energy with currents of 80-1000 pA). A sketch with the location of the sample respect to the beams can be seen in Figure 1. Samples were orientated such that the focused Ga^+ ion beam is at normal incidence to the cross-sectional surface (x-y plane) and SEM secondary electron (SE) images were taken of each sequential 2D slice (in the x-y plane) at a tilt angle of 54°. The image stretching caused by the tilt was automatically corrected by the microscope software and, therefore, all SEM images shown in this work have been tilt corrected. A beam current of 700 pA was used to carry out the sectioning.

Before sectioning, a protective coating of Carbon was deposited above the area of interest, then three staircase trenches were made in the front and at the sides of the volume of interest (see Figure 2). The front trench was made to reveal the cross-section containing the region of interest for subsequent imaging, and the two side ones to provide space to accommodate re-deposited materials during the sectioning process.

The 2D SE images were aligned and corrected for drift using cross-correlation of static features on the sample original surface following the method described in[9]. Then, an area containing the region of interest and with its top side coinciding with the sample's top surface is extracted from each image and arranged as a 3D dataset.

The 3D reconstruction was carried out using Mercury Software's Avizo .6.1. The different regions of interest appearing in the 2D images (e.g. metal, oxides, cracks,…) were automatically selected (using intensity thresholding methods) or

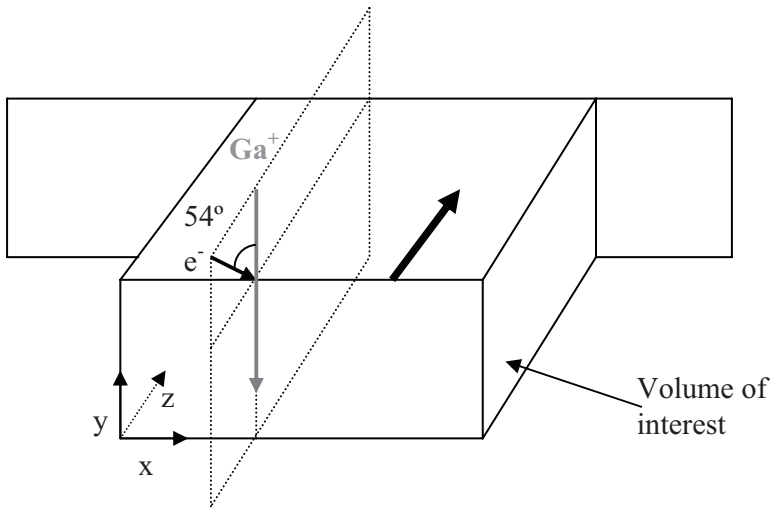

Figure 1: Diagram showing the volume of interest and the relative orientations of the e^- and Ga^+ beams. Sequential milling is performed on the x-y plane and along the z direction (thicker arrow).

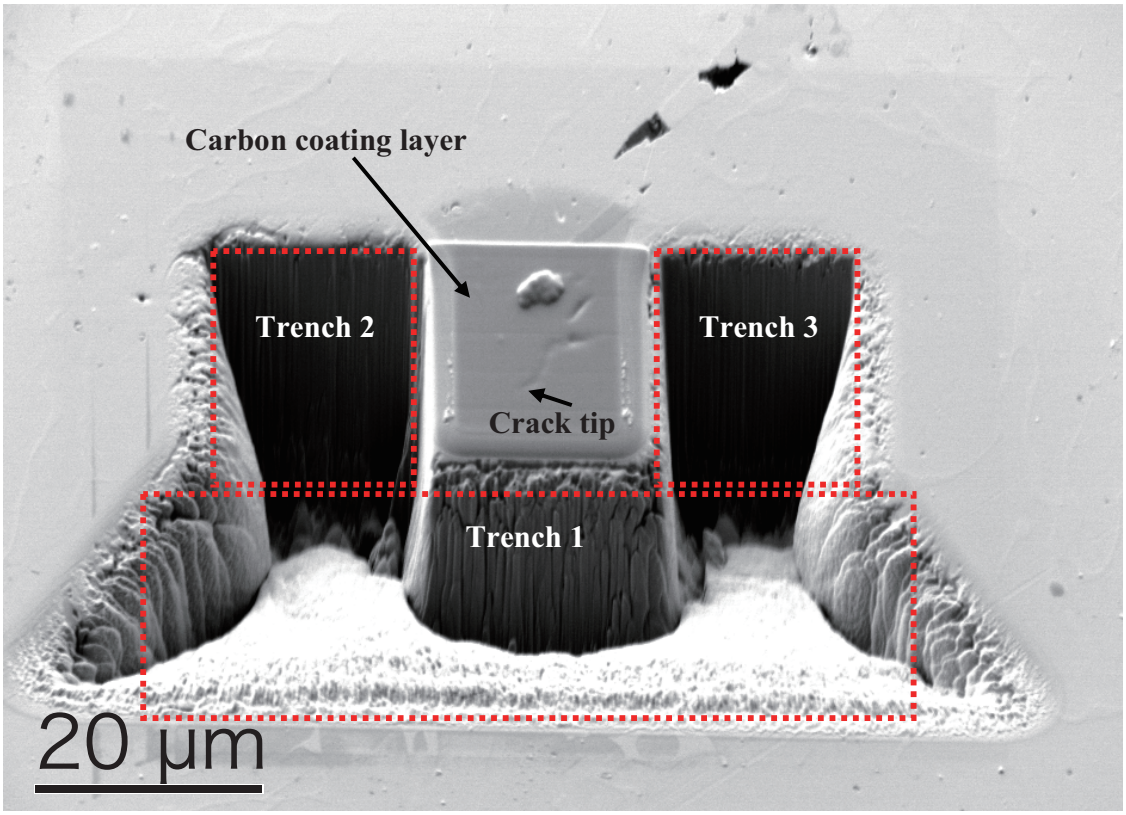

Figure 2: SEM SE image showing a general view of the welded 316L SS sample with the 3 trenches required to isolate the volume of interest and the protective carbon layer

manually drawn when no automated segmentation method was good enough to avoid the channelling contrast present in some SE images. The dimensions of the reconstructed volumes are typically ~20x20x5μm with a voxel size of ~11x11x40nm.

3. Results

3.1 Zr-alloy

The Zirconium alloy used for this study develops a layer of ZrO_2 oxide, exhibiting a characteristic breakaway behaviour [10] when exposed to PWR primary water for long periods. In the long term this leads to a loss of protectiveness at a thickness of just a few microns. It is therefore important to understand how the oxide layer develops if the oxidation mechanisms want to be understood. In particular, it is important to characterize the multiple cracks forming in the oxide and the morphology of the oxide/metal interface [11]. When designing the FIB sequential sectioning experiment, the acquisition time, brightness and contrast are optimized for revealing the features on the cross-sectional cut, as shown in Figure 3. The 3D reconstruction obtained from the whole series is shown in Figure 4. The oxide, as expected, contains many micro-cracks and the metal/oxide interface is not flat. In the inner and middle part of the oxide, the cracks are elongated along the direction parallel to the metal/oxide interface, while towards the oxide top, they are replaced by smaller round micro-pores. By looking at the 3D reconstruction, it was found that the micro-cracks near the metal/oxide interface are in most of the cases above the less oxidized portions of the interface, especially those near the metal/oxide interface.

Topography maps of the metal/oxide interface can be produced by projecting the 3D volume representing the metal along the y direction (normal to the sample surface) (see Figure 5). From this map, the roughness of the interface can be characterized by two parameters: the difference in height between the

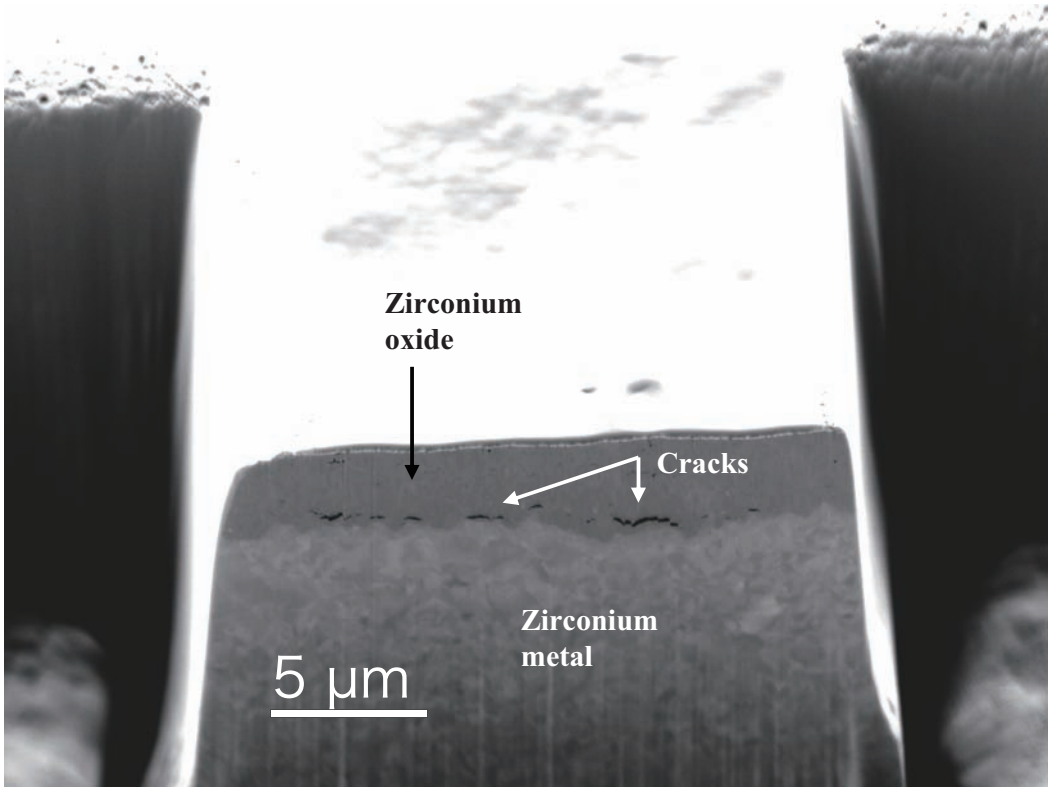

Figure 3: SEM SE image showing one of the first images from the 3D series in the Zr-alloy sample. Acquisition time, brightness and contrast were optimized to enhance the differences between the oxide, metal and cracks.

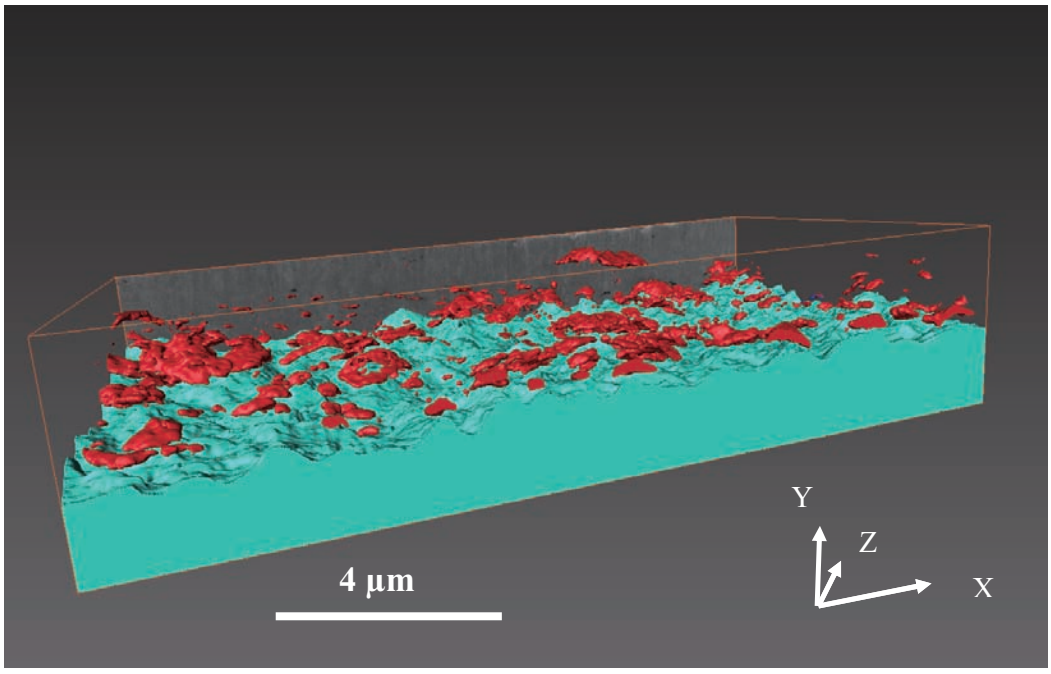

Figure 4: A snapshot of the reconstructed 3D volume containing the metal (blue) and the cracks in the zirconium oxide (red).

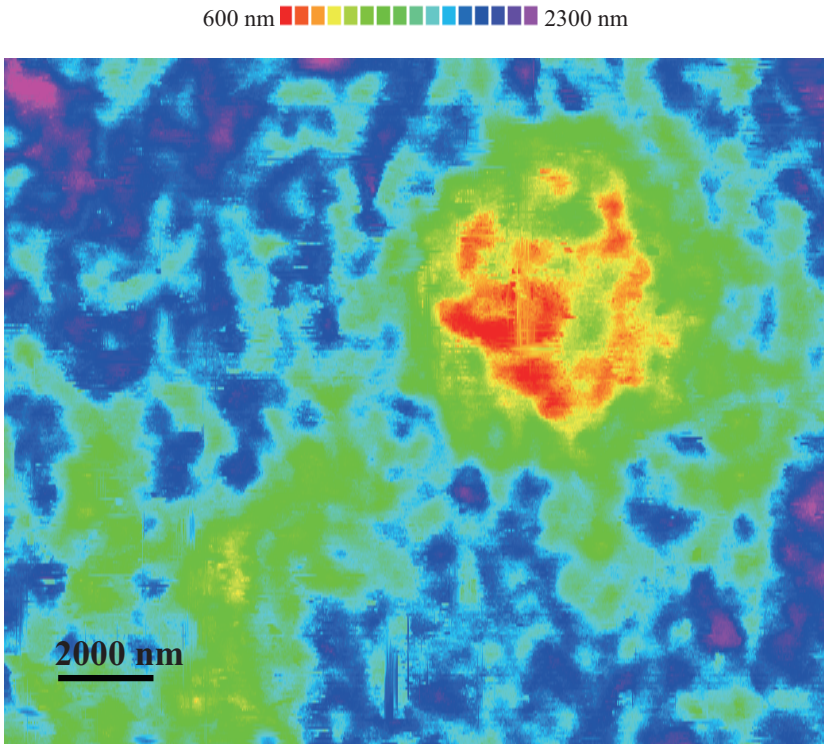

Figure 5: Metal/oxide interface topography maps in the Zr-alloy sample.

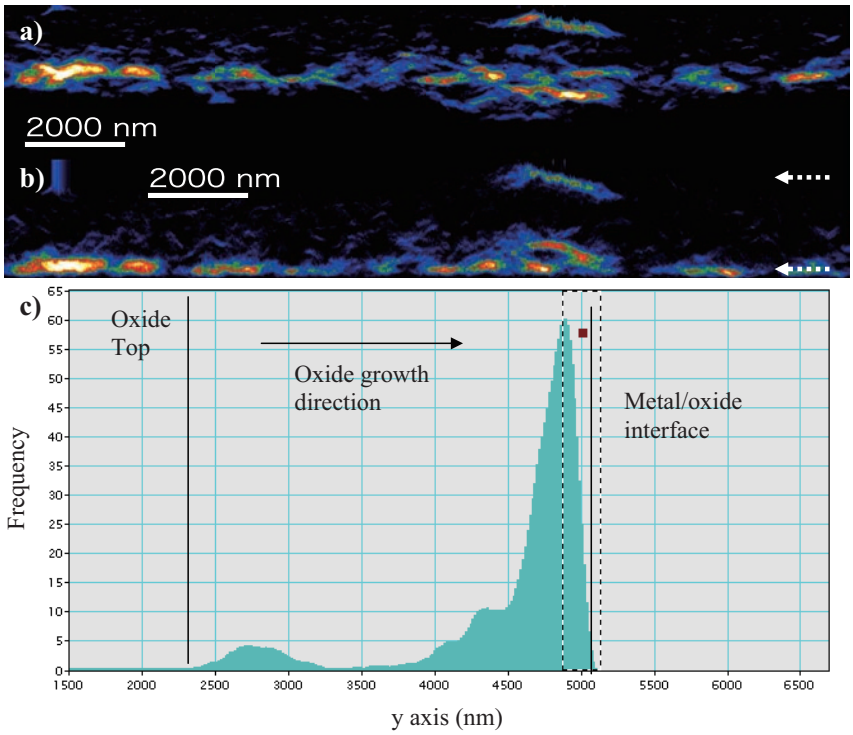

Figure 6: Characterization of the cracks in the black oxide. (a) Projected 2D image of the 3D reconstruction image along z direction, showing the distribution of the cracks in the oxide. (b) Same with (a), but with the metal/oxide interface being normalized to be a straight line as the bottom of the image. (c) Histogram of the Crack distribution along the growth direction.

highest point and the lowest point of the interface (with a maximum value of 1500nm and typical values of 350nm), and the standard deviation from the mean value of the interface height (RMS roughness, with a measured value of 200nm).

The projection of the 3D reconstruction image along z direction gives the distribution of cracks along the oxide growth direction (y direction), as shown in Figure 6a for the Zr oxide. It can be seen that the cracks appear to form a layer parallel to the metal/oxide interface, which becomes more well-defined in Figure 6b where the wavy interface has been normalized to make it flat. The layer of cracks has the first maximum at ~260 nm from the metal/oxide interface and a full width half maximum (FWHM) of ~320 nm (Figure 6c). Further away from the metal/oxide interface, only one single large crack is present at a distance about 400nm away from the oxide top (2.3μm from the metal/oxide interface). The location of this large crack coincides with the area with the lowest interface height, i.e. the deepest oxidized part.

3.2 304SS

Figure 7 shows one of the cross-sections produced during the milling series in the 304SS sample. As can be seen, exposure to the primary water produced a double oxide layer consisting of an outer Fe-rich spinel network of particles on the surface and an inner Cr-rich spinel layer[12]. Since the alloy was previously cold-worked, the oxidation process is more complex, and enhanced oxidation of twin deformation bands, high dislocation density regions and grain boundaries is observed[13]. The segmentation process, prior to the 3D reconstruction was performed manually and two materials were extracted: metal and oxide. In Figure 8a, the whole reconstructed volume can be observed (with the exception of the carbon coating layer, which has been artificially made transparent). In Figure 8b, the top 1μm of the reconstructed volume has been cropped (including the protective carbon coating layer, the Fe-rich spinel oxide particles and the bulk Cr-rich spinel oxide) in order to reveal the oxidized grain boundaries and deformation bands (they appear darker in the reconstruction). Note that this cropping (along the x-z plane) would be impossible experimentally since milling in the FIB is only along the x-y plane with the current sample geometry.

The bulk oxide and the oxidized features can be also extracted from the main volume for ease of observation, as can be seen in Figure 9. Once extracted, the 3D volume representing the location of the oxides can be binarized and projected along a direction parallel to the top bulk oxide layer (e.g the x-direction), as shown in Figure 10. This way, an easy representation of the extent of the oxidation can be obtained. If the isolated outer Fe-rich spinel particles are ignored, a depth profile representing the extent of oxidation can be integrated from Figure 10 and is shown in Figure 11. Position zero along the x axis represents the location of the original sample surface. The y-axis represents the percentage of sample surface that exhibits a certain depth of oxidation. A logarithmic scale has been used for this type of plots for ease of visualization.

Once the volume is segmented and reconstructed in 3D (e.g. as shown in Figure 9), individual features can be independently characterized. In Figure 12a, the plane containing the grain boundary arrowed in Figure 9 has been extracted from the SEM SE dataset. The oxidized portion of the grain boundary appears darker and it is not homogeneous in depth. The distribution of oxidation depths can be easily displayed as a histogram, as shown in Figure 12b.

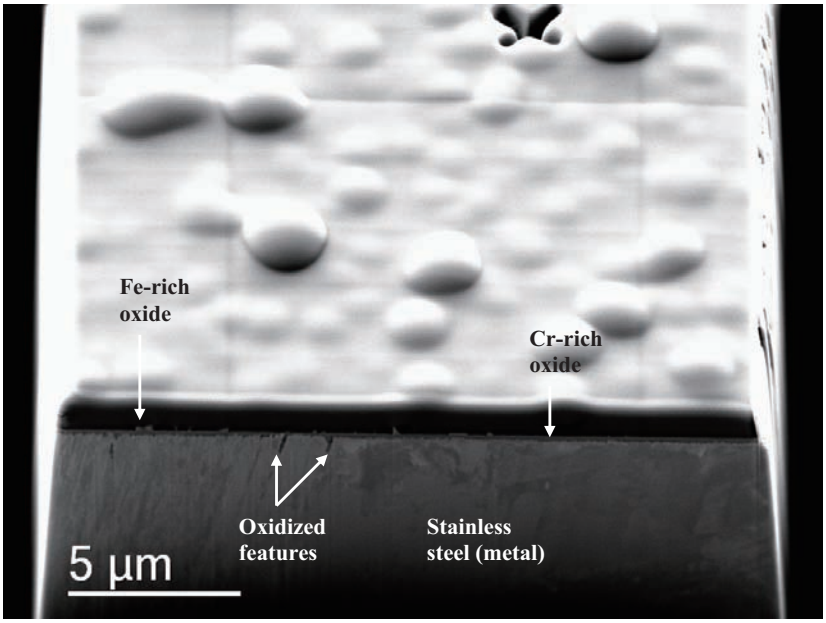

Figure 7: SEM SE showing one of the first images from the 3D series in the 304SS sample. Acquisition time, brightness and contrast were optimized to enhance the differences between the oxide and the metal.

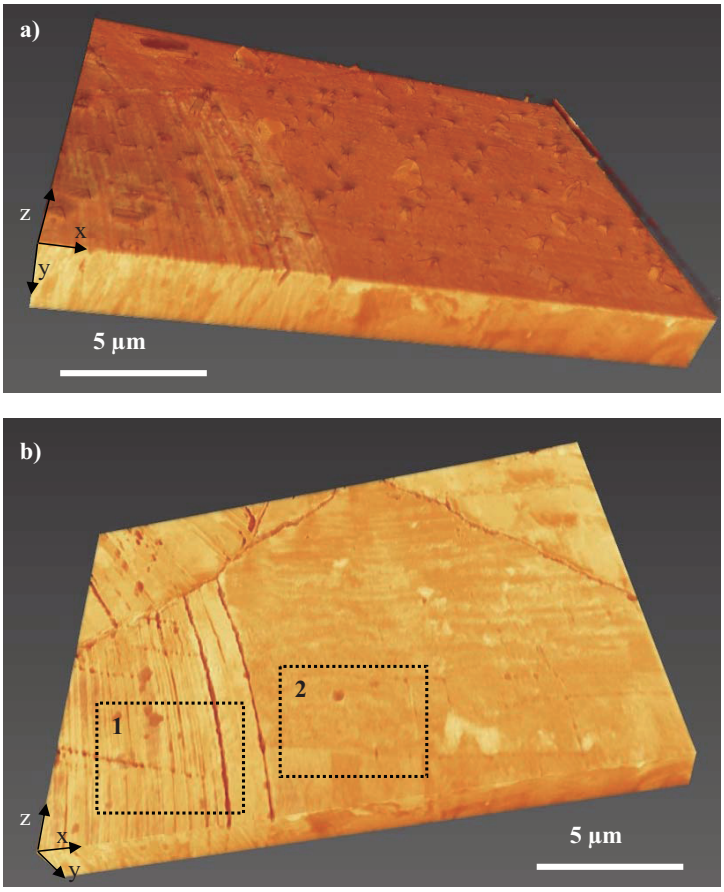

Figure 8: 3D reconstructed volumes before segmentation. (a) Whole 3D dataset without protective Carbon coating layer, where the Fe-rich spinel outer oxide particles are easily observed; (b) Same dataset as before but without the first top one micron (Protective carbon coating, Fe-rich spinel oxide particles and bulk Cr-rich spinel oxide have been removed). Labelled regions 1 and 2 have been separately analyzed and results shown in Figure 15.

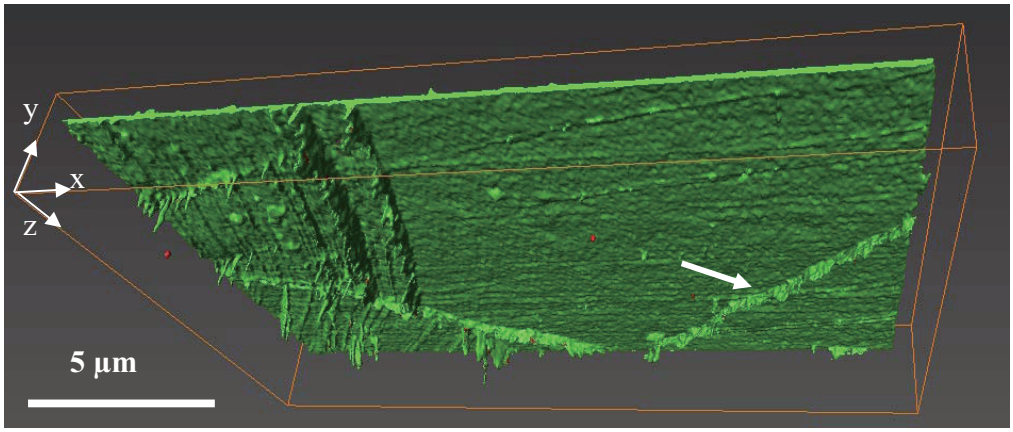

Figure 9: 3D reconstructed model showing the surface Cr-rich oxide spinel and the oxidized features. The model is displayed from underneath, so the original sample surface is on the opposite side.

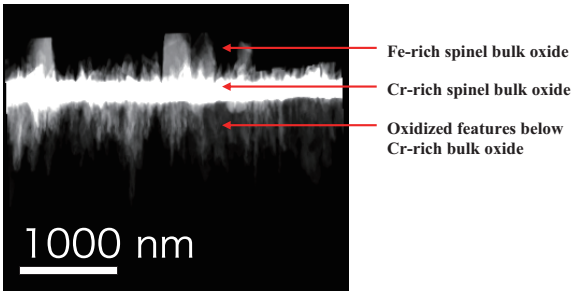

Figure 10: Projection along the x-direction (long side, parallel to original sample surface) of the model shown in Figure 9.

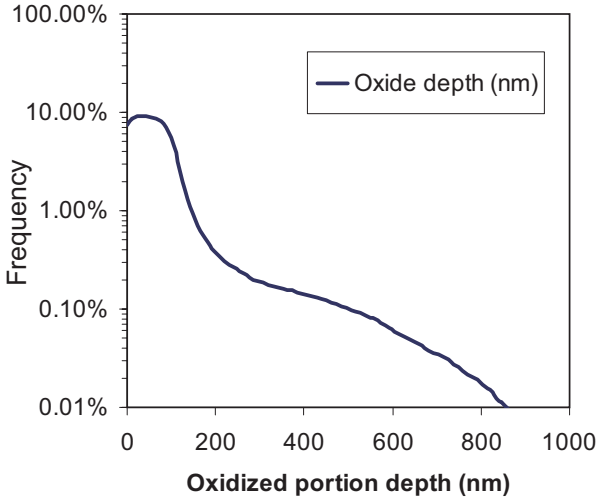

Figure 11: Histogram showing the depth of the oxidation observed for the whole 304SS sample.

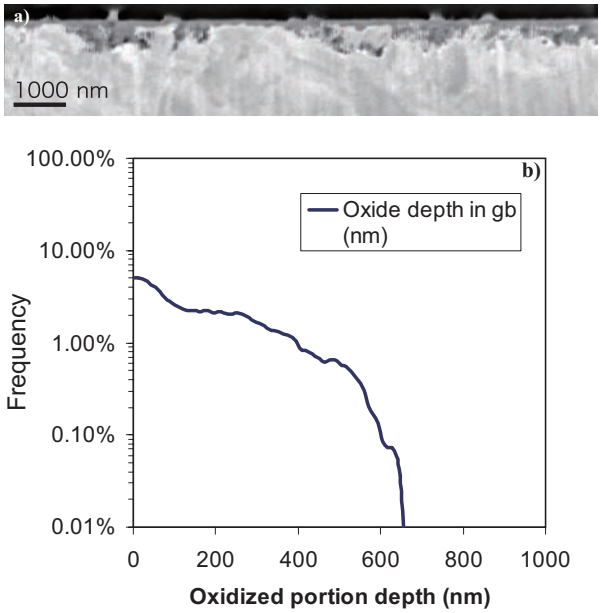

Figure 12: (a) SEM SE image reconstructed slice containing the arrowed grain boundary in Figure 9; (b) Histogram showing the depth of the oxidation observed along the grain boundary plane.

3.3 Welded 316L stainless steel sample

In Figure 2, a general view of the region chosen for the sequential sectioning was shown. In this region (coated with a carbon film), the tip of the crack observed on the top right part of the image was visible, and was chosen for the reconstruction. In the cross-sections used for the 3D reconstruction, several materials can be extracted, as seen in Figure 13. In this case, ferrite, austenite, open cracks and

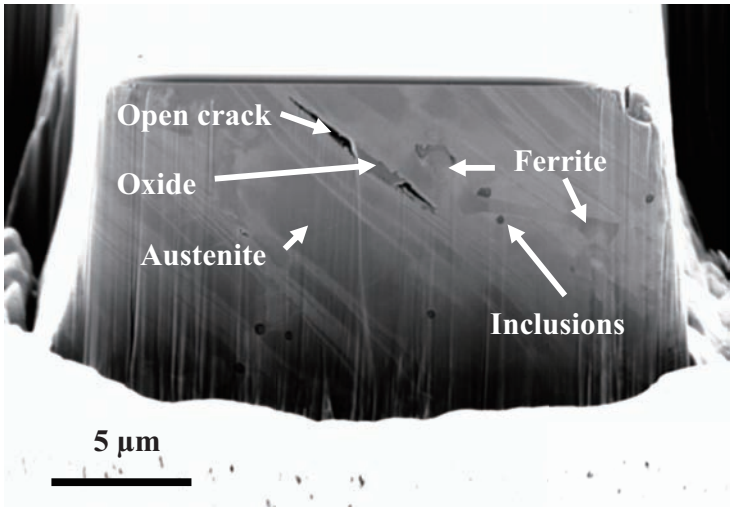

Figure 13: SEM SE showing one of the first images from the 3D series in the welded 316L SS sample. Acquisition time, brightness and contrast were optimized to enhance the differences between the different phases: ferrite, austenite, open crack, oxide and inclusion particles.

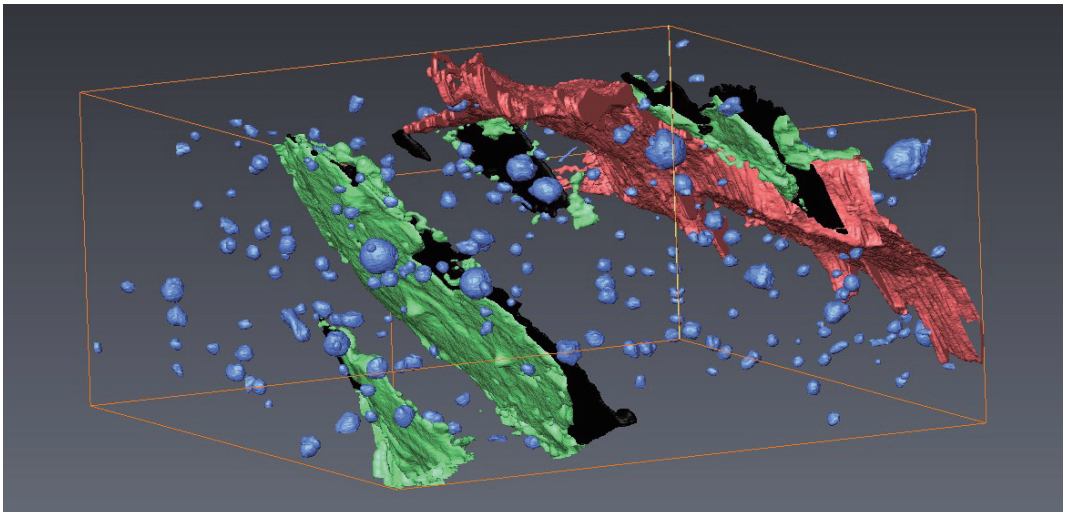

Figure 14: 3D reconstruction showing the different materials colour coded: inclusion particles are blue, oxides are green, open cracks are black and ferrite is red. Austenite has been omitted intentionally to ease the visualization.

oxide inside the cracks were manually segmented. The 3D reconstruction with all materials except the austenite can be seen in Figure 14. The oxide was found only filling the open cracks.

4. Discussion

By analyzing volumes of sizes ~20x20x5μm in 3D, a quantitative analysis on the morphology, size and location of various features ranging from nanometres to microns in size can be obtained with improved statistics. An adequate SEM image quality on the cross-sectional views was obtained when using a 700pA Ga^+ beam, which minimized the curtaining effect caused by preferential FIB milling when using higher currents and still allows the sequential milling acquisition to be obtained in hours. Material re-deposition was found to be a problem, but the prior milling of the side and front trenches created enough empty space around the analyzed volume to overcome it. With the chosen current (700pA) and a milling depth of 10μm (using Si as the material file),

curtaining was avoided up to depths of 6–7μm.

The 3D characterization of Zr oxides has proven very useful in order to get a clearer picture of how the cracks develop in 3D and whether they are correlated or not with the observed interface morphology. As can be seen in Figures 4 and 5, the interface roughness is considerable and, more importantly, as revealed after a careful study of the 3D model shown in Figure 4, it is correlated to the presence of cracks in the oxide (or viceversa). In order to get a more accurate representation of the distance between the cracks and the oxide/metal interface, the original projection along the z direction (Figure 6a) was normalized taking into account surface roughness (Figure 6b) and it was then clear that a very distinctive layer had formed at about 260nm from the interface. This is a very accurate way of characterizing the state of oxidation of the alloy, since the layers of thicker cracks seem to be correlated to the breakaway behaviour. It can also be seen that a second layer of cracks had already developed at 400nm from the oxide top or 2.3μm from the interface. The region where this earlier cracks developed has oxidized an average of 1μm than the rest of the sample analyzed (as shown in Figure 5), indicating that the sample does not oxidize homogeneously and it is likely to undergo the breakaway transitions locally.

The analysis of the surface oxides in the 304SS sample has revealed, in a very accurate way, how the prior cold work can change the oxidation resistance of the alloy. In the volume chosen for examination there are several grains, with different crystallographic orientations and which have developed twin deformation bands (typically along {111} planes). The oxidation depths histogram shown in Figure 11 represents the average oxidation behaviour but it is easy to see that this can be locally affected by factors such as grain orientation and whether or not the grain had developed deformation bands. For this reason, similar volumes in the regions marked as 1 and 2 in Figure 8b were individually analyzed following the method used to

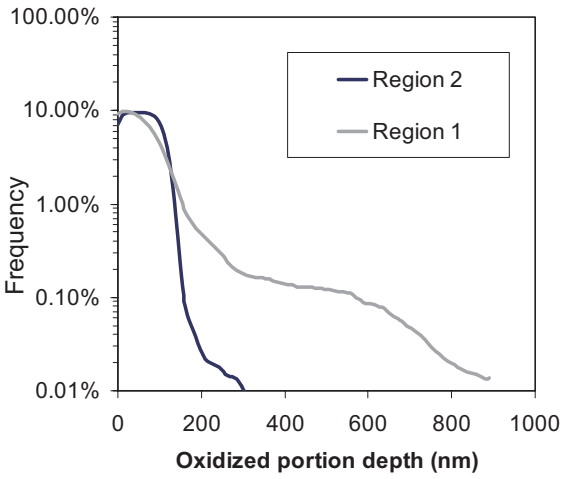

Figure 15: Histogram showing the depth of the oxidation observed for Regions 1 and 2 in Figure 8.

generate Figures 11 and 12. As it can be seen in Figure 15, the differences are obvious between the two regions. Region 2 shows an oxidation pattern more typical of non cold worked steels, with a homogeneous distribution of the oxidation, averaging ~150nm. On the other hand, Region 1 was chosen in a grain with many oxidized deformation bands and the distribution of oxidation depths is much wider and different from Region 2, with an average value of ~400nm. This type of differences would have been masked and averaged out if lower spatial resolution depth profiling techniques had been used for the characterization, e.g. Auger scanning microscopy or SIMS. TEM cross-sections would have overcome the spatial resolution problem and even improve it but would offer limited statistics.

The welded 316L SS sample was characterized in order to understand the cracking behaviour. In particular, it was important to check whether the crack propagated through or around the ferrite phase. The ferrite phase was particularly difficult to segmentate as it has a very similar composition to the austenite an only a slightly different channelling contrast could be used to isolate it. The segmentation, therefore, was entirely performed manually. As can be seen in Figure 16a, all the reconstructed cracks (black) and the associated oxide which

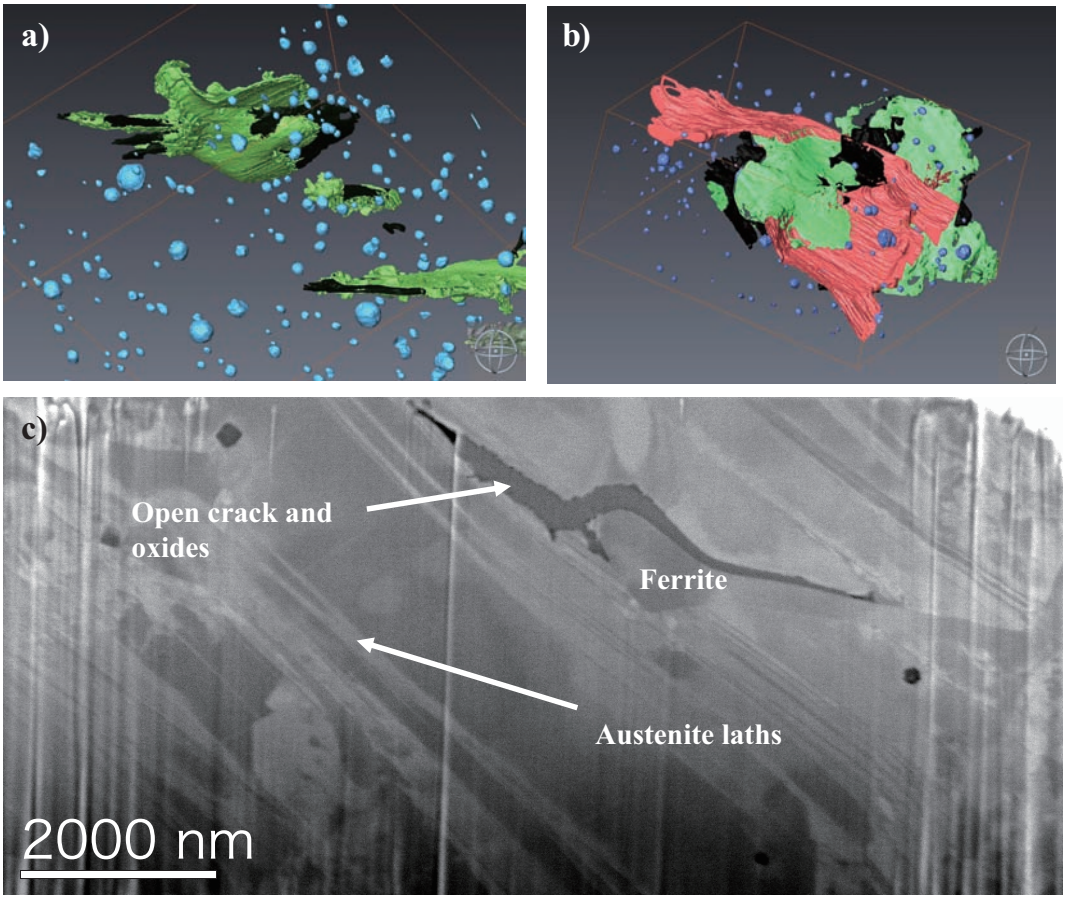

Figure 16: 3D models showing (a) cracks (black) and oxides in open cracks (green) growing parallel to the austenitic laths interfaces and (b) cracks and oxides in open cracks propagating around the ferrite phase (red). Inclusion particles are blue. (c) SEM SE image from serial sectioning showing how the crack grows around the ferrite phase

formed after the crack opened (green) are arranged in a somewhat parallel orientation to the austenitic laths planes. In Figure 16b it can be seen that the crack (black and green) seems to wrap the ferrite phase (red). This can be further check by looking at one of the original intermediate SEM SE images used to reconstruct the volume (Figure 16c). The inclusion particles (blue in Figures 16a and b) do not seem to play any particular role in the cracking mechanisms.

5. Conclusions

In this study, we have demonstrated that 3D FIB sequential sectioning is a very powerful technique capable of producing quick 3D models with nanometre resolution. Since contrast in SEM SE images can be correlated with differences in composition and/or crystallographic orientation/structure, it is usually possible to separate the different phases or regions of interest present in individual images. When this segmentation is applied to a series of images acquired after sequential milling, the different phases or features of interest can be then represented in 3D. With a serious of examples of application, we have demonstrated how novel statistical analysis on the 3D reconstructions can produce a series of quantitative data on the size and distribution of the analyzed features that adds a new dimension to our understanding of the different degradation mechanisms. It is expected that this method will become mainstream and part of any medium-high resolution analysis in 3D in the near future.

Acknowledgements

Sergio Lozano-Perez and Karen Kruska are grateful to INSS and the Department of Materials (University of Oxford) for sponsoring this research. Na Ni is grateful to the UK Engineering and Physical Sciences Research Council under grant EP/E036384/1 for sponsoring her Zr-alloy oxidation research.

References

(1) P. J. Withers, "X-ray nanotomography" Materials Today, 10 (2007), 26-34.

(2) A. King, G. Johnson, D. Engelberg *et al.*, "Observations of intergranular stress corrosion cracking in a grain-mapped polycrystal" Science 321 (2008), 382-385.

(3) V. A. Ignatova, S. V. D. Berghe, S. V. Dyck *et al.*, "Quantification problems in depth profiling of PWR steels using Ar/sup +/ ion sputtering and XPS analysis" Microscopy and Microanalysis 12 (2006), 432-437.

(4) M. Jacka, "Scanning Auger microscopy: Recent progress in data analysis and instrumentation" Journal of Electron Spectroscopy and Related Phenomena 114-116 (2001), 277-282.

(5) V. S. Smentkowski, S. G. Ostrowski, E. Braunstein *et al.*, "Multivariate statistical analysis of three-spatial-dimension TOF-SIMS raw data sets" Anal. Chem. 79 (2007), 7719-7726.

(6) S. Lozano-Perez, T. YamadaT. Terachi. in: "3-D Characterization of Crack Tips" *Proceedings of the Detection, Avoidance, Mechanisms, Modeling, and Prediction of SCC Initiation in Water-Cooled Nuclear Plants workshop*, 8-12 Sept, 2008.

(7) S. Lozano-Perez, D. W. Saxey, T. Yamada *et al.*, "Atom-probe tomography characterization of the oxidation of stainless steel" Scr. Mater. 62 (2010), 855-858.

(8) F. Elfallagh, B. J. Inkson, "Evolution of residual stress and crack morphologies during 3D FIB tomographic analysis of alumina" J. Microsc. 230 (2008), 240-251.

(9) B. Schaffer, W. Grogger,G. Kothleitner, "Automated spatial drift correction for EFTEM image series" Ultramicroscopy 102 (2004), 27-36.

(10) C. Lemaignan., in *Metals handbook. Vol. 13, Corrosion*, L. J. Korb, Ed. (Metals Park, Ohio: ASM International, Metals Park, Ohio, 1987), pp. 415.

(11) A. Yilmazbayhan, E. Breval, A. T. Motta et al., "Transmission electron microscopy examination of oxide layers formed on Zr alloys" J. Nucl. Mater. 349 (2006), 265-281.

(12) J. Robertson. in: "Modelling of corrosion and corrosion release in PWR primary circuits" *Water Chemistry of Nuclear Reactor Systems 5. Proceedings of the International Conference. Bournemouth, UK. Royal Soc. Chem. Eur. Nucl. Soc. Instn. Chem. Eng. 23-27 Oct. 1989*. 1989, 254.

(13) S. Lozano-Perez, M. Schröder, T. Yamada *et al.*, "Using NanoSIMS to map trace elements in stainless steels from nuclear reactors" App Surf Sci 255 (2008), 1541.